

# Anatomically based geometric modelling of the musculo-skeletal system and other organs

J. W. Fernandez, P. Mithraratne, S. F. Thrupp, M. H. Tawhai, P. J. Hunter

139

**Abstract** Anatomically based finite element geometries are becoming increasingly popular in physiological modelling, owing to the demand for modelling that links organ function to spatially distributed properties at the protein, cell and tissue level. We present a collection of anatomically based finite element geometries of the musculo-skeletal system and other organs suitable for use in continuum analysis. These meshes are derived from the widely used Visible Human (VH) dataset and constitute a contribution to the world wide International Union of Physiological Sciences (IUPS) Physiome Project ([www.physiome.org.nz](http://www.physiome.org.nz)). The method of mesh generation and fitting of tricubic Hermite volume meshes to a given dataset is illustrated using a least-squares algorithm that is modified with smoothing (Sobolev) constraints via the penalty method to account for sparse and scattered data. A technique (“host mesh” fitting) based on “free-form” deformation (FFD) is used to customise the fitted (generic) geometry. Lung lobes, the rectus femoris muscle and the lower limb bones are used as examples to illustrate these methods. Geometries of the lower limb, knee joint, forearm and neck are also presented. Finally, the issues and limitations of the methods are discussed.

## 1

### Background and previous work

The IUPS Physiome Project (Hunter et al. 2002) aims to promote anatomically and biophysically based computational modelling in order to understand physiological function in terms of underlying tissue and cellular structure mechanisms. This paper outlines the development of geometric models of organs and organ systems that can link to cell and tissue level properties. The geometries are being collected into hierarchical modelling ontologies (Hunter and Borg 2003) to facilitate data exchange among scientists contributing to the Physiome Project.

The Visible Human (VH) has become a common standard for researchers and provides a way of comparing and sharing geometries (Ackerman 1998). In the medical community there are numerous investigators who see the VH datasets as a standard for medical education and virtual simulation (Spitzer and Whitlock 1998). Other researchers who have used the VH datasets with anatomically based mechanics investigations include Dong et al. (2002) who segmented individual muscles and described fibre orientations for deformation analysis, and Hirota (2002) who used segmented VH geometry to model the contact mechanics of lower limb flexion.

In this paper we use cubic Hermite elements that differ from the usual Lagrangian finite elements in that they preserve both the continuity of the nodal values (C0 continuity), and their first derivatives (C1 continuity). This provides many advantages in constructing a finite element geometry, particularly of biological bodies such as muscles and other organs that typically have smooth surfaces. Moreover,

---

*Received: 31 January 2003 / Accepted: 13 September 2003*  
*Published online: 17 December 2003*

J. W. Fernandez (✉), P. Mithraratne, S. F. Thrupp  
M. H. Tawhai, P. J. Hunter  
Bioengineering Institute, The University of Auckland,  
Auckland, New Zealand  
E-mail: [jw.fernandez@auckland.ac.nz](mailto:jw.fernandez@auckland.ac.nz)

The authors would like to acknowledge the important input to this project from the members of the Bioengineering Institute, and the financial assistance from the Foundation for Research, Science and Technology New Zealand, and Marsden grant 01-UOA-070.

the realistic geometries are useful in such applications as virtual surgery and medical education. Another attractive feature of cubic Hermite elements is that fewer numbers of elements are required for complex geometries. **C1 interpolation** also provides a smooth change in the surface normal when sliding between element patches and this provides numerical benefits when solving contact mechanics problems (Wriggers et al. 2001; Stadler et al. 2003). Further, the interactions of bodies are more realistic than with linear meshes where obvious rigid gaps are a limitation of the low-order interpolation, highlighted in the modelling of fibre-reinforced sheets in contact (Christie 1997). In the literature, bicubic-Hermite elements have been used to construct the geometry of the human torso by fitting to data obtained from magnetic resonance imaging (MRI) scans (Bradley et al. 1997). They have also been used to describe the geometry and fibrous architecture of the heart (Nielsen et al. 1991). There are other types of **high-order interpolations that are useful, namely Besier functions and B-Splines** (Farin 1993), but since these have wider basis support, typically have non-nodally based degrees of freedom (dof), and often impose greater than C1 continuity (unless degree 2 B-Spline), which is not required or desirable in mechanics problems, they are less useful in continuum finite element analysis. (In finite elasticity problems we use the same basis functions for both geometry and solution, and it is desirable to have stress, which is related to the first derivative, continuous across elements, but not the second derivative.) Hence, we have **developed our software CMISS** (an interactive computer program developed by the Bioengineering Institute for Continuum Mechanics, Image analysis, Signal processing and System identification) to handle these cubic Hermite basis functions at all levels of the modelling process, from fitting and customisation to mechanics and post-processing, and we present numerical experiences with this interpolation scheme.

The **geometric fitting algorithm used** here is a variant of the well known **iterative closest point** (ICP) algorithm, where the surface fit is improved iteratively. There are various versions of this for fitting 3D geometric models (Rusinkiewicz and Levoy 2001). The implementation detailed here includes a Sobolev smoothing constraint for sparse and scattered data and has been previously illustrated for fitting anatomically based bicubic-Hermite surface meshes (Young et al. 1989; Bradley et al. 1997). Here, its implementation for fitting faces of 3D volume meshes is given.

Within the computer graphics and visualisation community, **FFD methods have been used extensively to customise models for animation or other morphing needs**. The separation of deformations into a local and global concept was first introduced by Barr (1984). Using these ideas a general deformation frame was introduced termed “free-form” deformation (FFD) and involved placing the object inside a trivariate tensor volume which was deformed, passing on the deformation to the object defined inside (Sederberg and Parry 1986). Various improvements have been presented over the years to the FFD idea and include extended-FFD (Coquillart 1990), rational-FFD (Kalra et al. 1992), direct-FFD (Hsu et al. 1992) and Dirichlet-FFD (Moccozet and Magnenat-Thalman 1997). Extended-FFD uses arbitrary shaped lattices that reflect the intended deformation rather than the standard parallelepiped lattice. Rational-FFD uses rational basis functions with the ability to place a weight on each control point providing an extra degree of freedom to manipulate the deformation. Direct-FFD reduces the confusion of moving many control points to target locations by deforming the control volume to minimise the desired control point changes in a “least-squares” sense. Dirichlet-FFD allows the user to place control points at arbitrary locations inside the control volume rather than just at lattice grid-points. Our technique draws ideas from all these methods in that we minimise the distance between arbitrary placed control points in a “least-squares” sense and have the ability to weight each control point. However, in our objective function, similar to the mesh fitting, a Sobolev smoothing term is used for additional control over the deformation of the control volume known as a “host mesh” in this paper.

Finally, although these techniques are common in the areas of computer graphics and vision, their use in biomechanical modelling is relatively new and we present numerical experiences and applications in this setting. This paper outlines the development of the geometric models and illustrates some clinical applications of the models.

## 2

### Volume meshes

The finite element meshes used in the present study are 3D volume meshes, and the interpolation or shape functions are **determined from the tensor product of 1D interpolation functions**. We shall therefore describe the 1D functions and infer their 3D counterparts. The element types presented here are categorised into two groups, namely, **tricubic** and **bicubic-linear elements**. In the former all **three directions are interpolated using cubic Hermite basis functions**, while in the latter, **two directions are interpolated using cubic Hermite interpolation and the third using linear Lagrange basis functions**. The four 1D cubic Hermite interpolation functions are

$$\begin{aligned}
\psi_1^0(\xi) &= 1 - 3\xi^2 + 2\xi^3 \\
\psi_2^0(\xi) &= \xi^2(3 - 2\xi) \\
\psi_1^1(\xi) &= \xi(\xi - 1)^2 \\
\psi_2^1(\xi) &= \xi^2(\xi - 1),
\end{aligned} \tag{1}$$

and the two linear Lagrange functions are given by

$$\begin{aligned}
\phi_1(\xi) &= 1 - \xi \\
\phi_2(\xi) &= \xi,
\end{aligned} \tag{2}$$

where  $\xi$  is the local or material coordinate with  $\xi \in [0,1]$ . Equations 1 and 2 are depicted in Fig. 1a and b, respectively. Interpolation of the global coordinates of line elements (Fig. 1c) with cubic Hermite basis functions is given by

$$\mathbf{u}(\xi) = \psi_1^0(\xi)\mathbf{u}_1 + \psi_2^0(\xi)\mathbf{u}_2 + \psi_1^1(\xi)\left.\frac{d\mathbf{u}}{d\xi}\right|_1 + \psi_2^1(\xi)\left.\frac{d\mathbf{u}}{d\xi}\right|_2, \tag{3}$$

where  $\mathbf{u}$  is  $x$ ,  $y$  or  $z$  and  $d\mathbf{u}/d\xi$  is the derivative of the global coordinate with respect to the local element coordinate  $\xi$ . Subscripts 1 and 2 refer to node numbers and superscripts 0 and 1 are the zeroth and first derivatives, respectively. The derivatives in Eq. 3 above can further be manipulated using the chain rule as

$$\mathbf{u}(\xi) = \psi_1^0(\xi)\mathbf{u}_1 + \psi_2^0(\xi)\mathbf{u}_2 + \psi_1^1(\xi)\left.\frac{d\mathbf{u}}{ds}\right|_1 \frac{ds}{d\xi} + \psi_2^1(\xi)\left.\frac{d\mathbf{u}}{ds}\right|_2 \frac{ds}{d\xi}. \tag{4}$$

The parameter  $s$  in Eq. 4 can, in general, be any measure of distance but here it is chosen to be the arc-length along the line. The scale factor  $L$  is therefore given by

$$\frac{ds}{d\xi} = \frac{\Delta s}{\Delta \xi} = \frac{L}{1.0} = L, \tag{5}$$

assuming the arc-length to be linear in  $\xi$ . Hence, the derivatives with respect to  $\xi$  in Eq. 3 are replaced with arc-length based derivatives and element scale factor  $L$ :

$$\mathbf{u}(\xi) = \psi_1^0(\xi)\mathbf{u}_1 + \psi_2^0(\xi)\mathbf{u}_2 + \psi_1^1(\xi)\left.\frac{d\mathbf{u}}{ds}\right|_1 L + \psi_2^1(\xi)\left.\frac{d\mathbf{u}}{ds}\right|_2 L. \tag{6}$$

Also note that the arc-length  $L$  is given by

$$L = \int_0^1 \sqrt{\left(\frac{dx}{d\xi}\right)^2 + \left(\frac{dy}{d\xi}\right)^2 + \left(\frac{dz}{d\xi}\right)^2} d\xi. \tag{7}$$

The non-linear Eq. 7 has to be solved iteratively in conjunction with Eq. 4 to determine the value for  $L$ . Additionally, a condition must also be placed on the arc-length derivatives to ensure we have continuity with respect to arc-length rather than  $\xi$ . At each node,  $n$ , the arc-length derivatives must have unit magnitude given by

$$\left\| \left( \frac{d\mathbf{u}}{ds} \right)_n \right\| = 1, \tag{8}$$

and can be achieved by normalising the arc-length derivatives. Further, when elements are connected, to ensure C1 continuity the  $\xi$  directions must be consistent from element to element and the scale factors at a node in one element should be the same as the scale factors for that node in another element. Therefore, a necessary condition for C1 continuity is that scale factors be nodally based. Any scale factor will meet this condition, but, to achieve a uniform spacing of  $\xi$  to arc-length, a good choice is to use the average arc-length from the surrounding elements as the scale factor at a node.

In linear Lagrange elements, only continuity of the nodal values is preserved across the element boundary. This therefore requires two element parameters (degrees of freedom) to describe the geometric variation in the line element. The element interpolation is given by

$$\mathbf{u}(\xi) = \phi_1(\xi)\mathbf{u}_1 + \phi_2(\xi)\mathbf{u}_2. \tag{9}$$

Bicubic-linear elements have 32 dof per coordinate per element. As shown in Fig. 2a, the interpolation in the  $\xi_3$  direction is linear. Thus an element consists of eight nodes with four parameters per

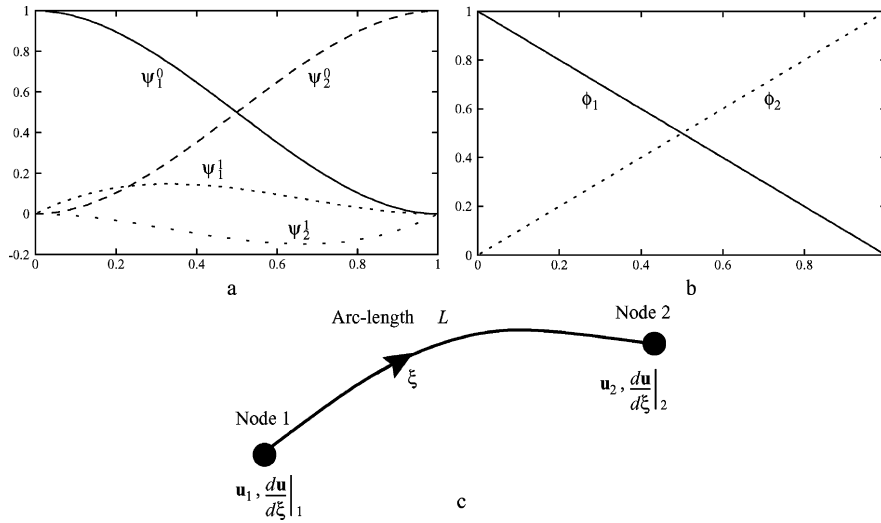


Fig. 1. a Cubic Hermite and b linear Lagrange basis functions. c Cubic Hermite line element

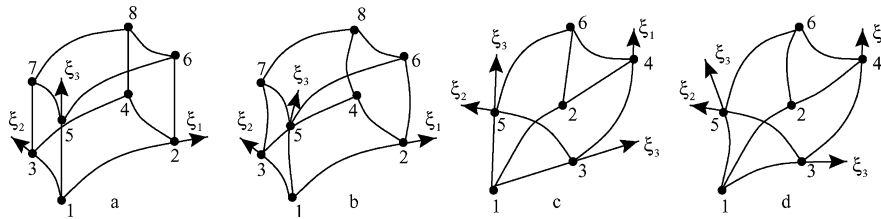


Fig. 2. a Bicubic-linear, b tricubic, c collapsed bicubic-linear and d tricubic volume elements

node. These consist of a nodal value, two first-order derivatives each in the  $\xi_1$  and  $\xi_2$  directions, and a cross-derivative. Tricubic volume elements (Fig. 2b) have 64 dof per coordinate per element (eight nodes with eight parameters per node). These parameters are: the nodal value, three first-order derivatives in each of three  $\xi$  directions, three second-order or cross-derivatives and a third-order (triple) derivative. It is sometimes convenient to construct a mesh with collapsed elements, such as in the case of a cylindrical body (rectus femoris muscle). Some nodes of the mesh are repeatedly used to define collapsed elements. In Fig. 2c, a bicubic-linear collapsed element is shown with six nodes. Nodes 1 and 2 are repeatedly used to define the element as 1–2–1–2–3–4–5–6 to comply with the other standard eight-noded elements in the mesh. Figure 2d illustrates a collapsed tricubic Hermite element.

### 3

#### Data digitisation

The soft tissue data for this study were collected from axial slices of the VH database (Fig. 3a, b). Data were collected from both the visible woman and man and used to fit the geometries. The digitisation process (creating discrete points in computer space from an image) was performed manually because of the detail of the images being collected. While bone is easy to differentiate from muscle, specific soft tissue identification was difficult, and at the time of creation, no software intelligent enough to perform this process was available to our knowledge. To aid in this process, movies of the images were generated to help identify the transition of tissue boundaries from slice to slice. For the bones of our mesh, we had available an anatomically accurate physical model (SOMSO, [www.somso.de](http://www.somso.de)), typically found in medical schools. A hand-held Polhemus Fastscan laser scanner (Applied Research Associates, NZ Ltd) was used to scan the surface (Fig. 3c, d).

### 4

#### Initial linear mesh

Two mesh designs were used to construct the linear meshes. Some bones and muscles were cylindrical in nature, such as the rectus femoris muscle and lower limb bones (femur, tibia and fibula), and therefore could be described simply by collapsed bicubic-linear elements (Fig. 2c). The centre nodes were generated as the mean of the surface nodes on an axial slice. In Fig. 4a, node 5 is the mean of

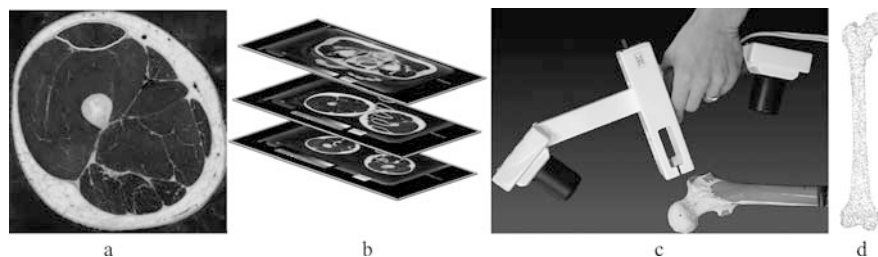


Fig. 3. a Visible human axial images, b muscle segmentation (Ackerman 1998), c Polhemus scanner scanning femur and d filtered digitised data

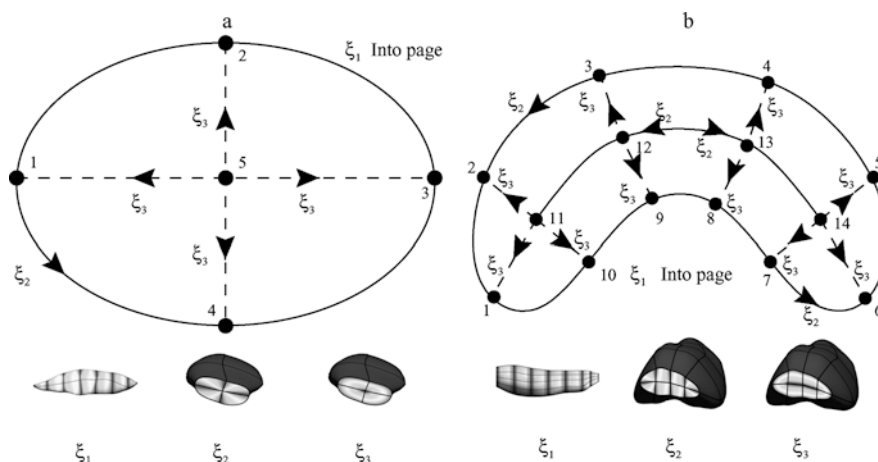


Fig. 4. Cross-section of a cylindrical mesh used for thin muscles and limb bones and b sheet mesh used for wrapping muscles

nodes 1...4. Other muscles were sheet-like and wrapped around bone. While collapsed elements could work in some cases, in highly curved muscles such as the quadriceps (thigh muscles), problems may arise with intersecting mesh lines. A solution to this was to use a combination of standard (Fig. 2a) and collapsed elements (Fig. 2c) as represented in Fig. 4b. The more curved the structure, the more standard elements can be used. Note that the  $\xi_2$  direction is going in opposite directions at the centre of the mesh and requires these degrees of freedom to be mapped together. The centre nodes were generated as follows, nodes 11...14 are the means of surface nodes 2 and 10, 3 and 9, 4 and 8, and 5 and 7 respectively. During the fitting process the centre nodes were kept fixed at these positions and therefore their degrees of freedom removed from the solution process. These are not the only designs possible and as more geometries are encountered different protocols will be established. Some of our future work involves automating the graphical user interface (CMGUI) of our software CMISS to generate these meshes automatically given a set of possible designs based on organ modelling experience.

Following these designs, two approaches could be used to construct the initial mesh. First, they may be constructed separately and then moved to coincide with the data points. This is practical where a physical model of the organ exists and the nodal points may be collected using a 3D digitising device. For the bones, a regular mesh was stencilled onto a SOMSO model (illustrated for the tibia, Fig. 5a) and the node points collected using a FARO arm (FARO Technologies, Inc., USA), with muscle insertion/origin patches collected at the same time (Fig. 5b).

Second, the mesh may be developed directly on the dataset by using some points as nodes of the mesh. The linear mesh topology is extracted from the cloud of data points by selecting data points on the outside of the data cloud. These serve as nodes for the linear meshes that are then used to generate elements in a systematic manner. The nodes are chosen to construct a regular mesh with a minimal number of elements required for fitting. This is the approach used for the muscles and lungs since physical models were not available. An advantage of this approach is that all collected organs were in the correct space and orientation relative to one another.

In Fig. 6a, b the data have been collected from images at 25 mm intervals in the longitudinal direction, since the geometric variation in this direction is minimal. Some of the data points at 50 mm

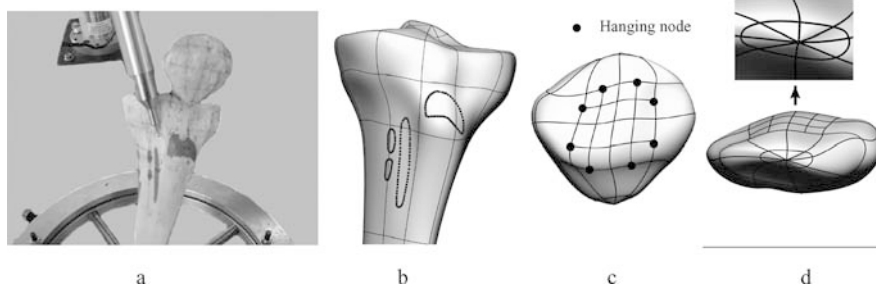


Fig. 5. **a** FARO arm digitising tibia nodes and muscle attachment patches, and **b** resulting mesh. **c** Refined patella with hanging nodes and **d** nodal derivative versions used for closing a mesh

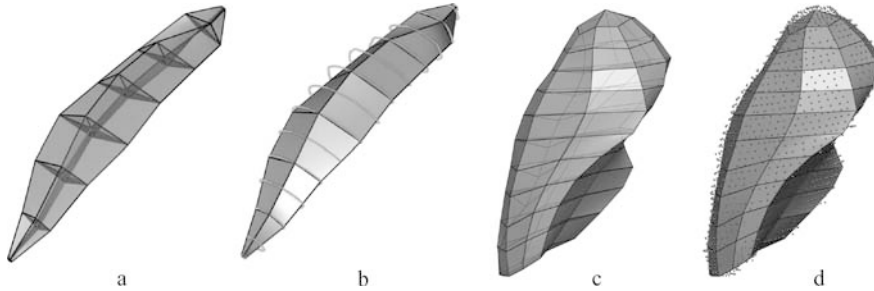


Fig. 6. **a** Initial trilinear mesh of rectus femoris muscle and **b** with data. **c** Initial trilinear mesh of left upper lobe (LUL), and **d** with data

intervals were used as nodes for the initial linear mesh. In the case of lung, however, images at 5 mm intervals were used to extract the spatial coordinates of the data points on the circumference of each lung lobe (Fig. 6c, d). This was required to capture surface curvature at places where the geometry was complex. This resulted in a relatively dense set of data compared to that obtained for the rectus femoris muscle. The nodes for the initial mesh were carefully placed to approximate the shape of the data.

Specific regions of the mesh required local refinement and this was accomplished in the regular mesh using hanging nodes (Stevens 2002), also known as improper or constrained nodes. The hanging nodes, illustrated for the patella (Fig. 5c, solid circles), have their nodal values and derivatives interpolated from the adjacent nodal values of the regular mesh. Note, however, that although the mesh appears smooth, strict C1 continuity is not maintained between elements at the hanging nodes. Moreover, in our implementation C1 continuity is not maintained on any irregular mesh, such as that seen in the lung mesh vertices (Fig. 6c, d), where three lines meet at one and while this is not desirable, it is not absolutely necessary at all regions of the mesh. For all bone meshes (femur, tibia, fibula and patella) the mesh topology required collapsing at the ends to close the mesh while maintaining a uniform  $\xi$  convention. This was achieved by using nodal derivative versions at a node and is illustrated for the patella in Fig. 5d. While regular meshes contain one derivative for each  $\xi$  direction, nodal versions allow multiple derivatives for each  $\xi$  direction. The patella in Fig. 5d has eight versions to maintain a smooth finish, but like the hanging nodes, C1 continuity is not enforced at the collapsed node.

## 5

### Face fitting of volume elements

Two approaches were implemented for fitting the geometry of a volume mesh to a given set of data. In the first method, objective functions are set up for each volume element of the mesh. The element objective function is basically the summation of the square of distances between each data point and its projection onto the element. The distance between a data point and its projection onto the element is a function of the element parameters as the projected point is obtained by interpolating the nodal parameters. Thus the parameters that minimise the objective function or in this case the “data error” are determined. The resulting element equations are then assembled to give the global mesh equations.

In the second approach, each volume element is decomposed into its faces and they are treated as area elements. For each face, an objective function is set up similar to that described earlier. Once the face equations are formulated, they are then assembled to give the global mesh equations. We used the

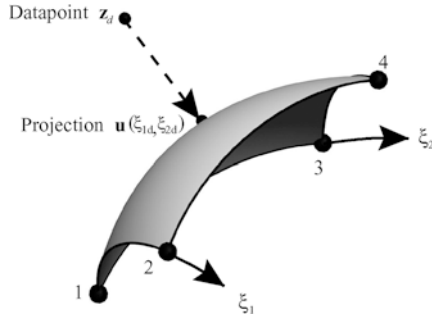


Fig. 7. Projection of data point  $\mathbf{z}_d$  onto an element face and resulting closest point  $\mathbf{u}(\xi_{1d}, \xi_{2d})$

second method to fit linear volume meshes to data. This method has an advantage over the former method as the projection of the data onto the mesh is always onto the external faces of volume meshes. In this way, mesh parameters associated with the interior nodes could be eliminated from the fitting problem. Moreover, the arc and surface curvature of faces of a volume mesh can be more easily controlled than in the first method.

## 6

### Data projection

The projection of a data point onto the face (Fig. 7) is obtained when the distance between the data point and its projection is minimum (i.e. the normal distance). Since the projection point lies on the face, its global coordinates could be expressed as a function of local face coordinates  $(\xi_1, \xi_2)$ , and face nodal parameters. A least-squares distance function,  $D$ , between a data point and its projection may be expressed by

$$D(\xi_1, \xi_2) = \|\mathbf{u}(\xi_1, \xi_2) - \mathbf{z}_d\|^2, \quad (10)$$

where  $\mathbf{z}_d$  is the spatial coordinates of the data point and  $\mathbf{u}(\xi_1, \xi_2)$  is interpolated using

$$\begin{aligned} \mathbf{u}(\xi_1, \xi_2) = & \psi_1^0(\xi_1)\psi_1^0(\xi_2)\mathbf{u}_1 + \psi_2^0(\xi_1)\psi_1^0(\xi_2)\mathbf{u}_2 \\ & + \psi_1^0(\xi_1)\psi_2^0(\xi_2)\mathbf{u}_3 + \psi_2^0(\xi_1)\psi_2^0(\xi_2)\mathbf{u}_4 \\ & + \psi_1^1(\xi_1)\psi_1^0(\xi_2)\left(\frac{\partial \mathbf{u}}{\partial \xi_1}\right)_1 + \psi_2^1(\xi_1)\psi_1^0(\xi_2)\left(\frac{\partial \mathbf{u}}{\partial \xi_1}\right)_2 \\ & + \psi_1^1(\xi_1)\psi_2^0(\xi_2)\left(\frac{\partial \mathbf{u}}{\partial \xi_1}\right)_3 + \psi_2^1(\xi_1)\psi_2^0(\xi_2)\left(\frac{\partial \mathbf{u}}{\partial \xi_1}\right)_4 \\ & + \psi_1^0(\xi_1)\psi_1^1(\xi_2)\left(\frac{\partial \mathbf{u}}{\partial \xi_2}\right)_1 + \psi_2^0(\xi_1)\psi_1^1(\xi_2)\left(\frac{\partial \mathbf{u}}{\partial \xi_2}\right)_2 \\ & + \psi_1^0(\xi_1)\psi_2^1(\xi_2)\left(\frac{\partial \mathbf{u}}{\partial \xi_2}\right)_3 + \psi_2^0(\xi_1)\psi_2^1(\xi_2)\left(\frac{\partial \mathbf{u}}{\partial \xi_2}\right)_4 \\ & + \psi_1^1(\xi_1)\psi_1^1(\xi_2)\left(\frac{\partial^2 \mathbf{u}}{\partial \xi_1 \partial \xi_2}\right)_1 + \psi_2^1(\xi_1)\psi_1^1(\xi_2)\left(\frac{\partial^2 \mathbf{u}}{\partial \xi_1 \partial \xi_2}\right)_2 \\ & + \psi_1^1(\xi_1)\psi_2^1(\xi_2)\left(\frac{\partial^2 \mathbf{u}}{\partial \xi_1 \partial \xi_2}\right)_3 + \psi_2^1(\xi_1)\psi_2^1(\xi_2)\left(\frac{\partial^2 \mathbf{u}}{\partial \xi_1 \partial \xi_2}\right)_4 \end{aligned} \quad (11)$$

with the derivatives with respect to  $\xi$  converted using

$$\left(\frac{\partial \mathbf{u}}{\partial \xi_\alpha}\right) = \left(\frac{\partial \mathbf{u}}{\partial s_\alpha}\right) \left(\frac{\partial s_\alpha}{\partial \xi_\alpha}\right),$$

and

$$\left(\frac{\partial^2 \mathbf{u}}{\partial \xi_\alpha \partial \xi_\beta}\right) = \left(\frac{\partial^2 \mathbf{u}}{\partial s_\alpha \partial s_\beta}\right) \left(\frac{\partial s_\alpha}{\partial \xi_\alpha}\right) \left(\frac{\partial s_\beta}{\partial \xi_\beta}\right),$$

for cross-derivatives (no sum on  $\alpha, \beta$ ). Note  $\mathbf{u}(\xi_1, \xi_2)$  here refers to the continuum field evaluated at material points  $\xi_1, \xi_2$ , while  $\mathbf{u}_n$  refers to the vector of nodal parameters used in the interpolation. Thus the local coordinates of the projection point  $(\xi_{1d}, \xi_{2d})$  and hence its global coordinates, can be determined by solving the following non-linear simultaneous equations using the Newton-Raphson procedure;

$$\frac{\partial D}{\partial \xi_1} = 0, \quad \frac{\partial D}{\partial \xi_2} = 0. \quad (12)$$

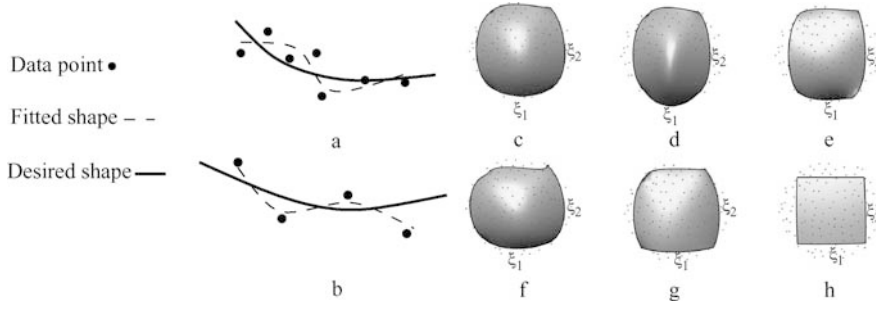


**Fig. 8.** Unbiased fitting caused by **a** scattered, and **b** sparse data. Effects of Sobolev weights with **c** no smoothing **d**  $\xi_1$  weighting on  $\alpha_1$  and **e** weighting on  $\alpha_1$  and  $\alpha_2$ . **f**, **g** show similar behaviour for the  $\xi_2$  direction and **h** shows weighting on all faces including the area term  $\alpha_5$

## 7

### Face objective function

The face objective function consists of two components, namely the data error and a smoothing constraint. The data error is the summation of the square of the distances between each data point and its projection while the latter is introduced to the objective function as a penalty function. The second order Sobolev norm (Bradley et al. 1997) is used as the smoothing constraint to account for sparse and scattered data. Figure 8a and b depict a mesh fitted with insufficient and scattered data without any smoothing constraints.

The complete objective function,  $F$ , of a face for a vector of nodal mesh parameters  $\mathbf{u}_n$  is given by,

$$F(\mathbf{u}_n) = \sum_{d=1}^N w_d \|\mathbf{u}(\xi_{1d}, \xi_{2d}) - \mathbf{z}_{2d}\|^2 + F_s(\mathbf{u}_n), \quad (13)$$

where  $\mathbf{z}_d$  are the geometric coordinates of data point  $d$ ,  $w_d$  is a weight for each data point,  $(\xi_{1d}, \xi_{2d})$  is obtained from the solution of Eqs. 10, 12 and  $\mathbf{u}(\xi_{1d}, \xi_{2d})$  is evaluated from Eq. 11.  $F_s(\mathbf{u}_n)$  is the Sobolev smoothing penalty function of the form,

$$F_s(\mathbf{u}_n) = \int_0^1 \int_0^1 \left\{ \alpha_1 \left\| \frac{\partial \mathbf{u}}{\partial \xi_1} \right\|^2 + \alpha_2 \left\| \frac{\partial \mathbf{u}}{\partial \xi_2} \right\|^2 + \alpha_3 \left\| \frac{\partial^2 \mathbf{u}}{\partial \xi_1^2} \right\|^2 + \alpha_4 \left\| \frac{\partial^2 \mathbf{u}}{\partial \xi_2^2} \right\|^2 + \alpha_5 \left\| \frac{\partial^2 \mathbf{u}}{\partial \xi_1 \partial \xi_2} \right\|^2 \right\} d\xi_1 d\xi_2, \quad (14)$$

where  $\alpha_i$  ( $i=1, \dots, 5$ ) are the Sobolev weights (penalty parameters). Each term has a distinct effect on the final shape of the fitted object. The first two terms ( $\alpha_1, \alpha_2$ ) control the arc-length, while the third and fourth terms ( $\alpha_3, \alpha_4$ ) control the arc-curvature in the  $\xi_1$  and  $\xi_2$  directions, respectively. The last term ( $\alpha_5$ ) represents the face area. For instance, if the weight associated with the cross-derivative term is set to a relatively higher value, one might end up with a smaller face area. All weights in Eq. 14 must be at least an order lower than the weight associated with the data error component  $w_d$  in Eq. 13, which is usually taken as 1.0. The effects of these parameters are illustrated for a simple 2D face in Fig. 8c–h. Figure 8c shows the effect with no smoothing. Placing weight on  $\alpha_1$  reduces the arc-length in the  $\xi_1$  direction (Fig. 8d) and including  $\alpha_3$  reduces the  $\xi_1$  curvature that is seen as a flattening in this direction (Fig. 8e). Similar behaviour is observed for the  $\xi_2$  direction (Fig. 8f, g). Placing weights on all coefficients including the area related term ( $\alpha_5$ ) causes a smooth reduction in the face area (Fig. 8h). The values used are shown in Table 1, but note that the magnitudes of these terms are larger than would be used in practice and are for emphasis of the effects only.

## 8

### Face equations

Face equations are formulated by differentiating the face objective function (Eq. 13) with respect to each face parameter and equating the resulting expression to zero. The scale factors (arc-lengths) are treated as constants during the process of differentiation to obtain a system of iterative linear equations, although they are functions of face parameters. In this way, solving a large number of non-linear equations, which is computationally expensive, can be avoided. For simplicity the formulation of the linear system is illustrated for a 1D element and the 2D/3D formulations can be inferred. Assuming for a 1D element (Fig. 1c) we have the closest projection point  $\xi_d$  for each data point  $\mathbf{z}_d$ . Differentiating the objective function (without the Sobolev term,  $F_s$ ) with respect to the nodal degrees of freedom (nodal values plus derivatives) and equating to zero gives



**Table 1.** Sobolev smoothing coefficients for data fitting

Sobolev smoothing coefficients					
Region	$\alpha_1$	$\alpha_2$	$\alpha_3$	$\alpha_4$	$\alpha_5$
Fig. 8c (2D face)	0.0	0.0	0.0	0.0	0.0
Fig. 8d (2D face)	0.5	0.0	0.0	0.0	0.0
Fig. 8e (2D face)	0.5	0.0	0.5	0.0	0.0
Fig. 8f (2D face)	0.0	0.5	0.0	0.0	0.0
Fig. 8g (2D face)	0.0	0.5	0.0	0.5	0.0
Fig. 8h (2D face)	2.0	2.0	2.0	2.0	2.0
Fig. 9a (rectus)	0.01	0.01	0.0005	0.0005	0.01
Fig. 9b (rectus)	0.0005	0.0005	0.0005	0.0005	0.0005
Fig. 9d (left upper)	0.0001	0.25	0.0001	0.25	0.5
Fig. 9d (left lower)	0.0001	0.05	0.0001	0.05	0.1
Fig. 9d (right upper)	0.01	0.05	0.01	0.05	0.1
Fig. 9d (right middle)	0.001	0.05	0.001	0.05	1.0
Fig. 9d (right lower)	0.01	0.5	0.01	0.5	1.0

$$\frac{\partial F}{\partial \mathbf{u}_n} = 2 \sum_{d=1}^N w_d \sum_{m=1}^4 \sum_{n=1}^4 (\psi_n(\xi_d) \mathbf{u}_n - z_d) \psi_m(\xi_d) = 0, \quad (15)$$

which leads to a global system of equations of the form  $A_{mn} \mathbf{u}_n = B_m$  where

$$A_{mn} = \sum_{d=1}^N w_d \sum_{m=1}^4 \sum_{n=1}^4 \psi_m(\xi_d) \psi_n(\xi_d), \quad (16)$$

$$B_m = \sum_{d=1}^N w_d \sum_{m=1}^4 \psi_m(\xi_d) z_d, \quad (17)$$

and  $N$  is the total number of data points. For the 1D element there are four (two nodal and two first-order derivative) parameters. Similarly the Sobolev smoothing term for a 1D element adds the following contribution to the linear system,

$$\frac{\partial F_s}{\partial \mathbf{u}_n} = 2 \int_0^1 \left\{ \beta_1 \frac{\partial \mathbf{u}_n}{\partial \xi} \frac{\partial \psi}{\partial \xi} + \beta_2 \frac{\partial^2 \mathbf{u}_n}{\partial \xi^2} \frac{\partial^2 \psi}{\partial \xi^2} \right\} d\xi, \quad (18)$$

which is numerically evaluated over the 1D line (or face in 2D/3D) using a scheme such as Gaussian quadrature. Here  $\beta_1$  refers to the  $\xi$  arc-length with  $\beta_2$  being the arc-curvature, which is different from the face parameters described earlier.

## 9

### Solving the fitting problem

Once the face equations are formulated for all the external faces of the mesh, they are then assembled to form the global equation set. Assemblage is carried out to satisfy continuity across the nodal values and their derivatives common to different faces (Sect. 2). The system of linear equations thus obtained is solved for the new mesh parameters and the new scale factors calculated (Eq. 7). The updated scale factors alter the shape of the mesh, since the scale factors are involved explicitly in the interpolation functions as detailed in Eq. 6. This, in turn, changes the optimum (minimum) value of the objective function described in Eq. 13. The objective function thus has a new optimum based on the current (solved) values of the mesh parameters. The steps described above are repeated for the next iteration to obtain the new optimum. The iterative procedure for the linear fitting is continued until the desired root mean square (RMS) error is attained. The RMS error of a fit for a 1D element is given by

$$RMS = \sqrt{\frac{\sum_{d=1}^N \|\mathbf{u}(\xi_d) - z_d\|^2}{N}}, \quad (19)$$

and the linear fitting algorithm is as follows:

1. Create an initial linear mesh from VH data points or using a FARO arm (Figs. 3 and 6).
2. Determine initial nodal scale factors (Eq. 7).
3. Determine data projections onto external mesh faces (Eq. 10) and initial data RMS error (Eq. 19).

- 4. Generate face equations using objective function defined in Eqs. 13 and 14 and solve.
- 5. Repeat the following steps until the data RMS is less than a set tolerance or a prescribed number of iterations is reached.
  - Update scale factors using new mesh parameters.
  - Project data onto new external faces.
  - Generate equations and solve.

**10**  
**Fitting results**

**10.1**  
**Rectus femoris**

The initial bicubic-linear mesh of the rectus femoris muscle was fitted to the VH data. All the elements are collapsed (Fig. 2c) at the  $\xi_3=0.0$  end. Directions  $\xi_1$  and  $\xi_2$  are interpolated using cubic Hermite basis functions while the  $\xi_3$  direction uses linear Lagrange basis functions. All the external faces therefore have bicubic interpolation. As can be seen from Fig. 9a, the density of data points in the  $\xi_1$  direction (bottom to top) is low compared to that in the  $\xi_2$  direction (anti-clockwise around muscle). This therefore requires higher weighting on the terms that control the arc-length and curvature in the  $\xi_1$  direction. Figure 9a shows the fitted bicubic-linear rectus femoris muscle with correctly weighted Sobolev smoothing. In contrast, a fitted mesh of the same muscle with unbiased Sobolev weights in both  $\xi_1$  and  $\xi_2$  is depicted in Fig. 9b. Because of insufficient data in the  $\xi_1$  direction, the fitted mesh has undesirable excessive curvature in the  $\xi_1$  direction.

**10.2**  
**Lung lobes**

All lung lobes were fitted with standard tricubic elements (Fig. 2b), except the left lower lobe (LLL) where two collapsed elements (Fig. 2d) have been used at the top to capture the correct shape outlined by the data. Sobolev weights were chosen to keep the surfaces smooth (Table 1). A fitted tricubic volume mesh of the left upper lobe (LUL) together with the data points is shown in Fig. 9c and Fig. 9d depicts all five lung lobes individually fitted. All simulations were performed on an IBM P690 1.3 GHz PV (White Plains, NY, USA), with simulations taking 10 and 45 s over four fits for the rectus muscle and four lung lobes respectively. A summary of mesh details, fitting RMS errors, and Sobolev smoothing coefficients are presented in Tables 1 and 2 respectively. Note that the RMS error reduces beyond four iterations, but the subjective quality of the mesh degrades.

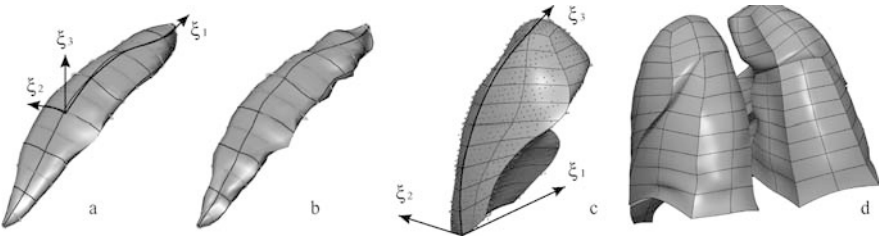


**Fig. 9.** Fitted bicubic-linear mesh of rectus femoris muscle with **a** correctly weighted and **b** unbiased weighted Sobolev smoothing. Fitted tricubic volume mesh of **c** left upper lobe and **d** complete lung lobes

**Table 2.** Mesh parameters and RMS data error

Mesh parameters				RMS data error (mm)				
Region	Nodes	Elements	Data points	Initial	Fit 1	Fit 2	Fit 3	Fit 4
Fig. 9a (rectus)	40	28	1607	2.35	1.83	1.62	1.43	1.32
Fig. 9d (left upper)	99	40	2252	2.93	2.02	1.89	1.61	1.50
Fig. 9d (left lower)	75	32	1823	3.02	1.64	0.89	—	—
Fig. 9d (right upper)	81	32	1723	2.97	1.80	1.69	—	—
Fig. 9d (right middle)	54	20	1116	2.40	1.56	1.37	—	—
Fig. 9d (right lower)	81	32	1615	3.61	3.07	2.78	2.44	—

Using the described methods, geometries of the lower limb (Fig. 10a–d), knee joint (Fig. 10e–h), skeleton (Fig. 10i), forearm (Fig. 10j) and shoulder, back and neck muscles (Fig. 10k, l) have been developed to date. Further regions are under development.

## 11

### Customisation: host-mesh fitting

The above finite element volume meshes have been developed by fitting linear meshes to a particular dataset. In practice, however, one might need to customise these geometric models to a set of data obtained from a different source or perhaps to a different scale (e.g. fitting to data from MRI or computed tomography (CT)). The “host-mesh” fitting method described below is a FFD technique used to perform geometric transformations consisting of both Euclidean (translation and rotation) and Affine (Euclidean plus scaling and shearing) operations on arbitrary finite element meshes.

The structure of the host mesh is a parallelepiped for all examples in this research, but can in general be any shape such as a cylinder. The size of the host mesh is derived from experience, however, as a general rule it should be close to the size of the object being deformed and the refinement of the host mesh depends on the control the user wishes to have over the deformation and object anatomy. For most cases one to three-element host meshes will suffice. For example, the femur is generally classed as having three regions (head, condyles and shaft, Fig. 13a), with separate control required at these locations so a three-element host mesh is suitable. Further work is being done to

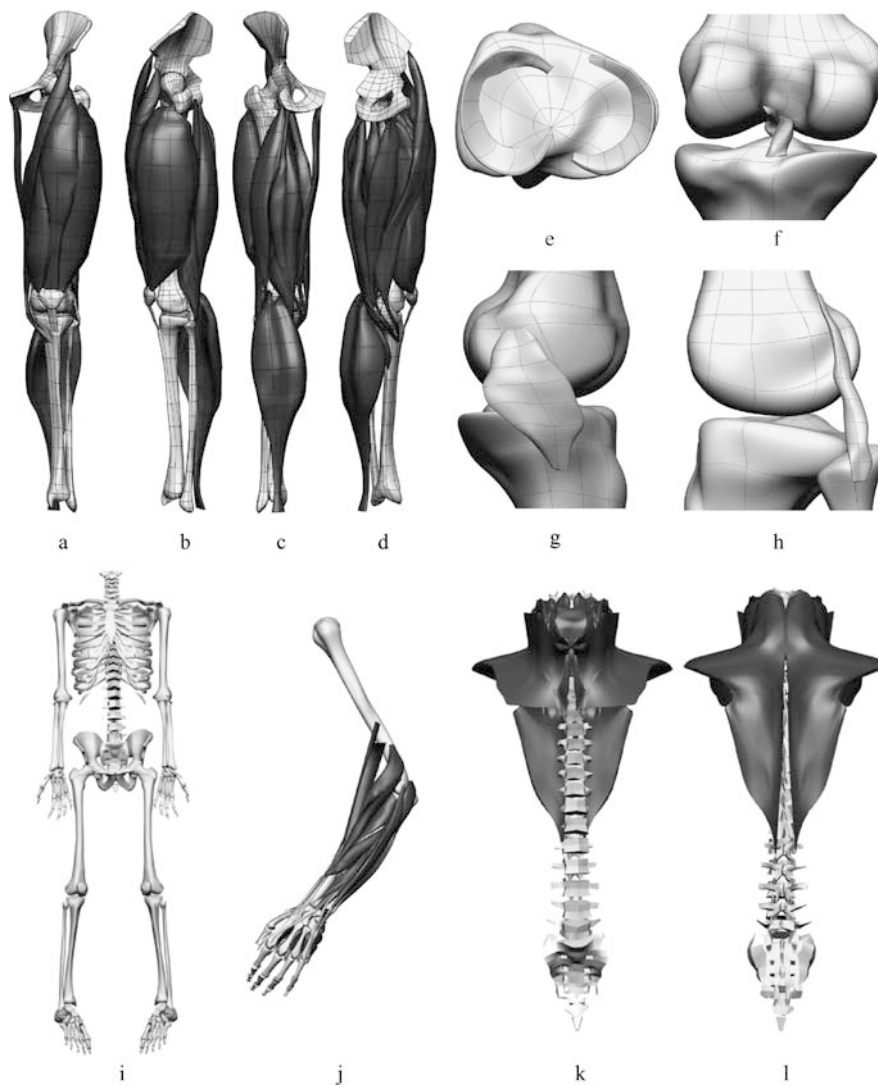


**Fig. 10.** The lower limb bones and skeletal muscles crossing the knee joint shown from **a** anterior, **b** lateral, **c** posterior, and **d** medial views. The knee joint showing: **e** the menisci, **f** the cruciate ligaments, **g** the tibial ligament, and **h** the fibular ligament. The skeleton frame **i** muscles of the **j** left forearm and **k**, **l** the muscles of the neck, shoulder and back from the anterior and posterior respectively

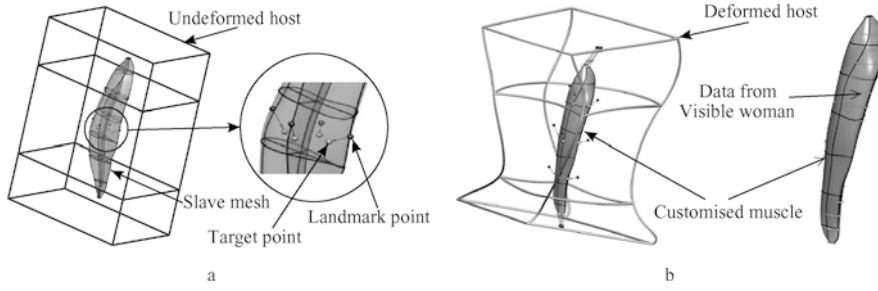


**Fig. 11. a** Undeformed host mesh with slave mesh and landmark points embedded within. The corresponding target points are indicated. **b** Deformed host and customised muscle with data points

analyse the sensitivity of different shapes and sizes on the same deformation. The mesh that needs to be transformed, also known as the slave mesh, is completely embedded in a host mesh. The latter, in general, is a tricubic volume mesh consisting of fewer elements. Figure 11a shows a slave mesh (generic rectus femoris muscle) embedded in a host mesh with three tricubic volume elements. Landmark (initial) and target (final) points are needed to perform the transformation. Each landmark point has a target defined by considering the geometrically important locations of the slave mesh. In general, these landmark/target pairs are chosen as unique features of the organ that are easily identifiable from medical images such as CT or MRI. A higher number of control (landmark/target) points leads to a more accurate transformation and the appropriate number of control points must be subjectively determined. Once the required landmark and target points are obtained, the host mesh is deformed to minimise the objective function given in Eq. 13, where  $\mathbf{z}_d$  are the global target points and the landmark points  $\mathbf{u}(\xi_{1d}, \xi_{2d}, \xi_{3d})$  are interpolated using 3D basis functions derived in a similar manner to the 2D basis functions in Eq. 11.  $F_S(\mathbf{u}_n)$  is now a 3D smoothing constraint and contains more terms with new definitions for the Sobolev constraints,  $\gamma_i$  ( $i=1, \dots, 10$ ), and is given by,

$$\begin{aligned}
 F_S(\mathbf{u}_n) = & \int_0^1 \int_0^1 \int_0^1 \left\{ \gamma_1 \left\| \frac{\partial \mathbf{u}}{\partial \xi_1} \right\|^2 + \gamma_2 \left\| \frac{\partial \mathbf{u}}{\partial \xi_2} \right\|^2 + \gamma_3 \left\| \frac{\partial \mathbf{u}}{\partial \xi_3} \right\|^2 \right. \\
 & + \gamma_4 \left\| \frac{\partial^2 \mathbf{u}}{\partial \xi_1^2} \right\|^2 + \gamma_5 \left\| \frac{\partial^2 \mathbf{u}}{\partial \xi_2^2} \right\|^2 + \gamma_6 \left\| \frac{\partial^2 \mathbf{u}}{\partial \xi_3^2} \right\|^2 \\
 & + \gamma_7 \left\| \frac{\partial^2 \mathbf{u}}{\partial \xi_1 \partial \xi_2} \right\|^2 + \gamma_8 \left\| \frac{\partial^2 \mathbf{u}}{\partial \xi_2 \partial \xi_3} \right\|^2 + \gamma_9 \left\| \frac{\partial^2 \mathbf{u}}{\partial \xi_3 \partial \xi_1} \right\|^2 \\
 & \left. + \gamma_{10} \left\| \frac{\partial^3 \mathbf{u}}{\partial \xi_1 \partial \xi_2 \partial \xi_3} \right\|^2 \right\} d\xi_1 d\xi_2 d\xi_3,
 \end{aligned} \quad (20)$$

where  $\gamma_i$  ( $i=1, \dots, 3$ ) are the three arc-lengths,  $\gamma_i$  ( $i=4, \dots, 6$ ) are the three curvatures in the  $\xi_1, \xi_2, \xi_3$  directions respectively and  $\gamma_i$  ( $i=7, \dots, 9$ ) are the three surface area terms for faces  $(\xi_1-\xi_2)$ ,  $(\xi_2-\xi_3)$  and  $(\xi_3-\xi_1)$ , while  $\gamma_{10}$  is related to the volume. Moreover,  $\gamma_{10}$  ensures the shape of the original volume is not too distorted after fitting. Although it appears that smoothing is not required to minimise the error between the landmark and target points, it is sometimes useful to control the excessive deformation of the host to ensure that the new mesh does not become unphysiologically distorted.

## 12

### Nodal values of the transformed slave

Since the slave is completely embedded in the host, its nodal coordinates can be readily defined by the local coordinates and the nodal parameters (mesh dof) of the host. Moreover, any deformation that the host mesh undergoes results in a similar deformation in the slave although the relative positions of the slave nodes remain unchanged. Thus, once the new mesh parameters of the deformed host are determined, the nodal values of the transformed slave are updated by substituting the local coordinates into the host interpolation functions and deformed host parameters.

## 13

### First derivatives of the transformed slave

The slave mesh is embedded inside the host, hence its material coordinates  $(\eta_1, \eta_2, \eta_3)$  can be defined as a function of the host material coordinates  $(\xi_1, \xi_2, \xi_3)$  through:

$$\begin{aligned}
 \eta_1 &= f(\xi_1, \xi_2, \xi_3) \\
 \eta_2 &= f(\xi_1, \xi_2, \xi_3) \\
 \eta_3 &= f(\xi_1, \xi_2, \xi_3).
 \end{aligned} \quad (21)$$

Further, based on Eq. 21, first derivatives of global coordinates of the slave can be given by

$$\frac{\partial \mathbf{u}}{\partial \eta_1} = \frac{\partial \mathbf{u}}{\partial \xi_1} \frac{\partial \xi_1}{\partial \eta_1} + \frac{\partial \mathbf{u}}{\partial \xi_2} \frac{\partial \xi_2}{\partial \eta_1} + \frac{\partial \mathbf{u}}{\partial \xi_3} \frac{\partial \xi_3}{\partial \eta_1}, \quad (22)$$

$$\frac{\partial \mathbf{u}}{\partial \eta_2} = \frac{\partial \mathbf{u}}{\partial \xi_1} \frac{\partial \xi_1}{\partial \eta_2} + \frac{\partial \mathbf{u}}{\partial \xi_2} \frac{\partial \xi_2}{\partial \eta_2} + \frac{\partial \mathbf{u}}{\partial \xi_3} \frac{\partial \xi_3}{\partial \eta_2}, \quad (23)$$

$$\frac{\partial \mathbf{u}}{\partial \eta_3} = \frac{\partial \mathbf{u}}{\partial \xi_1} \frac{\partial \xi_1}{\partial \eta_3} + \frac{\partial \mathbf{u}}{\partial \xi_2} \frac{\partial \xi_2}{\partial \eta_3} + \frac{\partial \mathbf{u}}{\partial \xi_3} \frac{\partial \xi_3}{\partial \eta_3}. \quad (24)$$

Expanding Eq. 22 and writing it in matrix form gives

$$\begin{bmatrix} \frac{\partial x}{\partial \xi_1} & \frac{\partial x}{\partial \xi_2} & \frac{\partial x}{\partial \xi_3} \\ \frac{\partial y}{\partial \xi_1} & \frac{\partial y}{\partial \xi_2} & \frac{\partial y}{\partial \xi_3} \\ \frac{\partial z}{\partial \xi_1} & \frac{\partial z}{\partial \xi_2} & \frac{\partial z}{\partial \xi_3} \end{bmatrix} \begin{bmatrix} \frac{\partial \xi_1}{\partial \eta_1} \\ \frac{\partial \xi_2}{\partial \eta_1} \\ \frac{\partial \xi_3}{\partial \eta_1} \end{bmatrix} = \begin{bmatrix} \frac{\partial x}{\partial \eta_1} \\ \frac{\partial y}{\partial \eta_1} \\ \frac{\partial z}{\partial \eta_1} \end{bmatrix}. \quad (25)$$

The RHS vector of Eq. 25 contains the nodal first derivatives with respect to one of its local coordinates  $\eta_1$ . The coefficient matrix is the Jacobian matrix of the host at the slave node under consideration. The unknowns in the equation remain unchanged before and after the deformation of the host and they can be determined using the undeformed host and original slave parameters. Once Eq. 25 is solved for the unknowns, they can be substituted back to obtain the first derivatives of the transformed slave at the slave nodes as follows

$$\begin{bmatrix} \frac{\partial x}{\partial \eta_1} \\ \frac{\partial y}{\partial \eta_1} \\ \frac{\partial z}{\partial \eta_1} \end{bmatrix}_T = \left[ \frac{\partial(x, y, z)}{\partial(\xi_1, \xi_2, \xi_3)} \right]_U^{-1} \left[ \frac{\partial(x, y, z)}{\partial(\xi_1, \xi_2, \xi_3)} \right]_D \begin{bmatrix} \frac{\partial x}{\partial \eta_1} \\ \frac{\partial y}{\partial \eta_1} \\ \frac{\partial z}{\partial \eta_1} \end{bmatrix}_O, \quad (26)$$

where  $\left[ \frac{\partial(x, y, z)}{\partial(\xi_1, \xi_2, \xi_3)} \right]$  is the Jacobian matrix of the host and subscripts T, U, D and O represent the transformed slave, undeformed host, deformed host and original (untransformed) slave, respectively. The new nodal cross-derivatives of the transformed slave can be obtained using a similar approach but is more mathematically involved. The derivation of expressions for the second derivatives is detailed in Appendix A.

## 14

### Soft tissue examples

#### 14.1

##### Example 1

The rectus femoris muscle presented here was fitted to data obtained from the visible man anatomical sections. A similar set of data was derived for the same muscle from the visible woman images. Of the data available, 24 pairs of landmark and target points were identified for the customisation of the fitted rectus femoris muscle of the visible man to the visible woman data. Figure 11a depicts the generic muscle embedded in the undeformed host mesh together with the landmark and corresponding target points. The deformed host mesh with the customised or transformed muscle is shown in Fig. 11b. Sobolev smoothing was increased in the longitudinal  $\xi_1$  arc-length and curvature ( $\gamma_1$  and  $\gamma_4$ , Eq. 20) and on the volume coefficient  $\gamma_{10}$  and are given in Table 3. This was to ensure that the new muscle did not appear too oscillatory in texture. In order to assess how well the customisation performs with the above-explained technique, the data obtained from the visible woman sections were compared with the transformed muscle. The data from the visible woman images closely follow the customised muscle as shown in Fig. 11b. A check of the goodness of the fitting problem is the RMS of the landmark/target pairs after fitting. For the rectus femoris example the RMS was 1.80 mm. Further, the RMS for the deformed muscle and complete visible women data was 2.56 mm indicating a reasonable fit to the entire dataset while only using relatively few dof.

#### 14.2

##### Example 2

The lung lobes were fitted individually and therefore the fitted meshes may have spurious gaps or overlapping between them. The “host mesh” technique was used to bring the fitted lobes into proper contact. Fig. 12a shows the LLL embedded in a host mesh with the landmark and target points. The

**Table 3.** Sobolev smoothing coefficients for host-mesh examples

Sobolev smoothing host-mesh examples					
Region	$\gamma_1$	$\gamma_2$	$\gamma_3$	$\gamma_4$	$\gamma_5$
	$\gamma_6$	$\gamma_7$	$\gamma_8$	$\gamma_9$	$\gamma_{10}$
Fig. 11 (rectus)	0.005	0.0001	0.0001	0.005	0.0001
Fig. 12 (lungs)	0.0001	0.0001	0.0001	0.0001	0.005
	0.0001	0.0001	0.0001	0.0001	0.0001
Fig. 13a–d (femur)	0.0001	0.0001	0.0001	0.0001	0.0001
	0.005	0.0001	0.0001	0.005	0.0001
	0.0001	0.0001	0.0001	0.0001	0.005

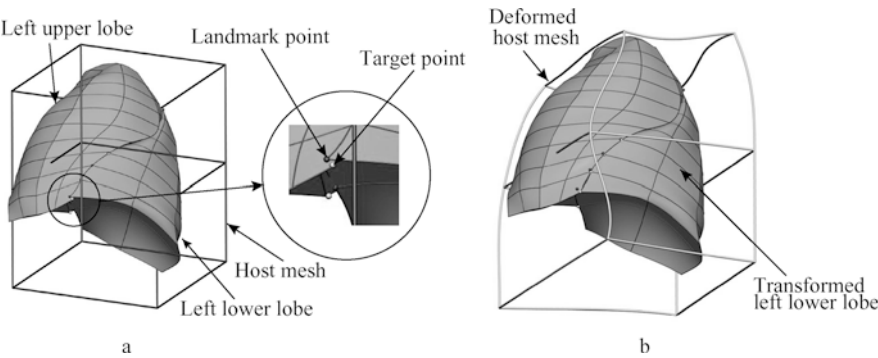


**Fig. 12.** **a** Left lower lobe with host mesh and defined landmark/target points and **b** transformed left lower lobe and deformed host

LUL is shown to indicate the target surface. The landmark points were chosen from the nodes of the fitted LLL and the target points were then determined to get proper contact with the faces of the LUL. A Sobolev value of 0.0001 was used for all coefficients ( $\gamma_i$ ,  $i=1, \dots, 10$ , Table 3). The transformed LLL with its deformed host is depicted in Fig. 12b.

Using the same computer as for the fitting algorithm, the customisation of both the rectus muscle and lung lobes took 2 s each. While these simulations were performed on a high performance computer using the Auckland Bioengineering Institute’s finite element software CMISS, it is our intention to highlight the method in this paper, rather than the processing speed, which may be adapted to other platforms.

## 15 Bone examples

The articular profile of bone geometry is linked to the stress distribution. The generation of patient-specific bone geometry is therefore of great interest to orthopaedic surgeons and other medical professionals interested in computer models of patient cases. Moreover, the alteration of bone geometry is commonly used in surgery to reduce zones of high stress gradients. Here we illustrate two examples of bone customisation that are of clinical interest.

### 15.1 Example 3

In Fig. 13a a generic femur is embedded in a three-element host mesh giving separate control of the three main regions (head, shaft, condyles). Key landmark points, easily identified by a surgeon (i.e. bone extremities) are stored with the bone as material points (Fig. 13b). A cloud of points obtained from a cadaver is overlayed and the host transformed (Fig. 13c) to match the identical points from the dataset. The new bone is shown in Fig. 13d and the Sobolev weights used shown in Table 3.

### 15.2 Example 4

Figure 13e and f illustrate a surgical technique known as a Maquet’s procedure (Maquet 1984), which involves the arterial displacement of the tibial tuberosity (the small bump on the tibia

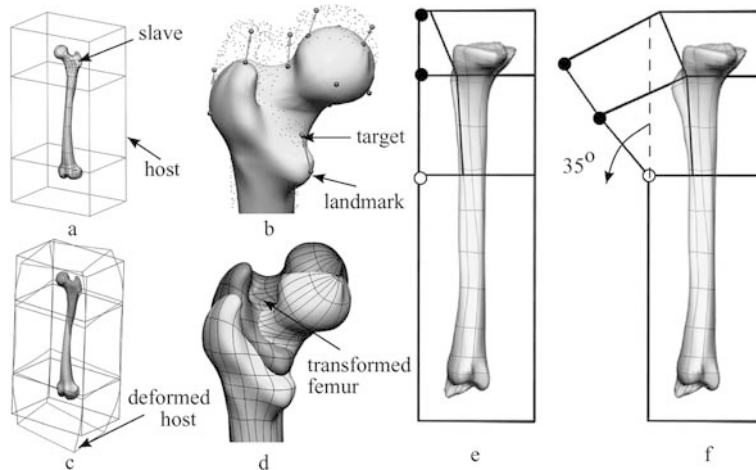


**Fig. 13.** a A generic femur embedded in a host with b landmark and target points, c the deformed host and d the transformed femur. A Maquet's procedure showing the e before and f after results of the anterior displacement of the tibial tuberosity. The solid nodes of the mesh are rotated 35° about the hollow node

where the patella-tendon attaches). The aim is to reduce the patello-femoral articulation stress by elevating forward the attachment site of the patella-tendon. The new bone shape can be derived from a generic one by using a simple five-element host mesh (Fig. 13e). All nodes of the host are fixed except those highlighted (*solid circles*, Fig. 13e). Rather than minimising control points using a least-squares procedure, the nodes are rotated about a centre of rotation (*hollow circle*, Fig. 13f). The deformation is therefore kept to a localised region, and no Sobolev smoothing is required.

## 16

### Discussion and model limitations

The construction of anatomically based 3D volume meshes using cubic Hermite interpolation has been illustrated, providing realistic geometry. Further, a customising procedure “host-mesh” fitting, based on FFD is illustrated for use with such cubic Hermite elements and illustrated in a biomechanics and clinical setting. This technique allows global customisation with relatively few control points, thus eliminating the need to refit the entire mesh. While this procedure is straightforward, the logistics of creating a host mesh and selecting customisation points is still a manual procedure. These procedures require automation to make the process more user friendly. This method also requires that the original mesh be similar to the desired final configuration for subjectively acceptable results. Further, the selection of the control points and fitting can be aided by automatic segmentation tools. A future goal of this work is to assimilate this software with an MRI device to develop a complete medical tool. The meshes demonstrated here have been designed for application to mechanics problems; in particular, for the solution of finite elasticity problems. A problem that is typically encountered during mesh creation is that multiple bodies do not conform and may overlap. This was seen for the lung lobes, and is due to the smoothing in fitting and manual placement in space. A further problem is that the meshes may have been constructed from organ data that was not in the state required. For example, the VH lungs were more collapsed than is normal in the functioning lung. For the meshes to be useful, they may require initial deforming to a more correct state. We have investigated the application of contact constraints being added to the fitting objective function. While this would prevent bodies from penetrating one another, it does not account for the material properties of each body. The contact constraints are currently being tested as part of the governing equations of mechanics instead so that bodies may interact given their material properties. The results of this study shall be reported in a future communication. The use of cubic Hermite basis functions to some extent limits our flexibility in mesh design, local region customisation, irregular refinement and generally restricts the number of topologies we can describe. An alternative approach is “subdivision surfaces” (Schroder and Zorin 1998) in conjunction with any arbitrary mesh topology composed of triangles or quadrilaterals. These surfaces achieve C2 continuity on regular meshes and C1 on irregular meshes with local mesh control and have significant advantages for geometric surface representation. It is not clear, however, that it is suitable for solving the governing equations from physical conservation laws, which is the main use for the geometric models considered in this paper and further investigation is required.

## Appendix A

Differentiating Eq. 22 with respect to  $\eta_2$  gives,

$$\begin{aligned} \frac{\partial^2 \mathbf{u}}{\partial \eta_1 \partial \eta_2} &= \frac{\partial \mathbf{u}}{\partial \xi_1} \frac{\partial^2 \xi_1}{\partial \eta_1 \partial \eta_2} + \frac{\partial \xi_1}{\partial \eta_1} \frac{\partial^2 \mathbf{u}}{\partial \xi_1 \partial \eta_2} + \\ &\quad \frac{\partial \mathbf{u}}{\partial \xi_2} \frac{\partial^2 \xi_2}{\partial \eta_1 \partial \eta_2} + \frac{\partial \xi_2}{\partial \eta_1} \frac{\partial^2 \mathbf{u}}{\partial \xi_2 \partial \eta_2} + \\ &\quad \frac{\partial \mathbf{u}}{\partial \xi_3} \frac{\partial^2 \xi_3}{\partial \eta_1 \partial \eta_2} + \frac{\partial \xi_3}{\partial \eta_1} \frac{\partial^2 \mathbf{u}}{\partial \xi_3 \partial \eta_2}. \end{aligned} \quad (27)$$

In Eq. 27, the terms on the RHS underlined with a single line are the unknowns needed to be solved. The terms with double under lines are however “mixed derivatives” and are not desirable in the current form. They can further be manipulated in the following manner using the chain rule:

$$\begin{aligned} \frac{\partial^2 \mathbf{u}}{\partial \xi_1 \partial \eta_2} &= \frac{\partial}{\partial \eta_2} \left( \frac{\partial \mathbf{u}}{\partial \xi_1} \right) \\ &= \frac{\partial^2 \mathbf{u}}{\partial \xi_1^2} \frac{\partial \xi_1}{\partial \eta_2} + \frac{\partial^2 \mathbf{u}}{\partial \xi_1 \partial \xi_2} \frac{\partial \xi_2}{\partial \eta_2} + \frac{\partial^2 \mathbf{u}}{\partial \xi_1 \partial \xi_3} \frac{\partial \xi_3}{\partial \eta_2}, \end{aligned} \quad (28)$$

$$\begin{aligned} \frac{\partial^2 \mathbf{u}}{\partial \xi_2 \partial \eta_2} &= \frac{\partial}{\partial \eta_2} \left( \frac{\partial \mathbf{u}}{\partial \xi_2} \right) \\ &= \frac{\partial^2 \mathbf{u}}{\partial \xi_2^2} \frac{\partial \xi_2}{\partial \eta_2} + \frac{\partial^2 \mathbf{u}}{\partial \xi_1 \partial \xi_2} \frac{\partial \xi_1}{\partial \eta_2} + \frac{\partial^2 \mathbf{u}}{\partial \xi_2 \partial \xi_3} \frac{\partial \xi_3}{\partial \eta_2}, \end{aligned} \quad (29)$$

$$\begin{aligned} \frac{\partial^2 \mathbf{u}}{\partial \xi_3 \partial \eta_2} &= \frac{\partial}{\partial \eta_2} \left( \frac{\partial \mathbf{u}}{\partial \xi_3} \right) \\ &= \frac{\partial^2 \mathbf{u}}{\partial \xi_3^2} \frac{\partial \xi_3}{\partial \eta_2} + \frac{\partial^2 \mathbf{u}}{\partial \xi_1 \partial \xi_3} \frac{\partial \xi_1}{\partial \eta_2} + \frac{\partial^2 \mathbf{u}}{\partial \xi_2 \partial \xi_3} \frac{\partial \xi_2}{\partial \eta_2}. \end{aligned} \quad (30)$$

All the terms on the RHS of Eqs. 28, 29 and 30 are known. For instance, terms like  $\partial \xi_i / \partial \eta_2$  ( $i=1, \dots, 3$ ) can be evaluated using Eq. 25 and the other terms such as  $\partial^2 \mathbf{u} / \partial \xi_i \partial \xi_j$  ( $i=1, \dots, 3, j=1, \dots, 3, i \neq j$ ) are readily available either from undeformed or deformed host geometry. Expanding Eqs. 28, 29 and 30 and putting into matrix form gives,

$$\begin{bmatrix} \frac{\partial(x, y, z)}{\partial(\xi_1, \xi_2, \xi_3)} \end{bmatrix} \begin{bmatrix} \frac{\partial^2 \xi_1}{\partial \eta_1 \partial \eta_2} \\ \frac{\partial^2 \xi_2}{\partial \eta_1 \partial \eta_2} \\ \frac{\partial^2 \xi_3}{\partial \eta_1 \partial \eta_2} \end{bmatrix} = [R], \quad (31)$$

where

$$[R] = \begin{bmatrix} \frac{\partial^2 x}{\partial \eta_1 \partial \eta_2} - \frac{\partial \xi_1}{\partial \eta_1} \frac{\partial^2 x}{\partial \xi_1 \partial \eta_2} - \frac{\partial \xi_2}{\partial \eta_1} \frac{\partial^2 x}{\partial \xi_2 \partial \eta_2} - \frac{\partial \xi_3}{\partial \eta_1} \frac{\partial^2 x}{\partial \xi_3 \partial \eta_2} \\ \frac{\partial^2 y}{\partial \eta_1 \partial \eta_2} - \frac{\partial \xi_1}{\partial \eta_1} \frac{\partial^2 y}{\partial \xi_1 \partial \eta_2} - \frac{\partial \xi_2}{\partial \eta_1} \frac{\partial^2 y}{\partial \xi_2 \partial \eta_2} - \frac{\partial \xi_3}{\partial \eta_1} \frac{\partial^2 y}{\partial \xi_3 \partial \eta_2} \\ \frac{\partial^2 z}{\partial \eta_1 \partial \eta_2} - \frac{\partial \xi_1}{\partial \eta_1} \frac{\partial^2 z}{\partial \xi_1 \partial \eta_2} - \frac{\partial \xi_2}{\partial \eta_1} \frac{\partial^2 z}{\partial \xi_2 \partial \eta_2} - \frac{\partial \xi_3}{\partial \eta_1} \frac{\partial^2 z}{\partial \xi_3 \partial \eta_2} \end{bmatrix} \quad (32)$$

Equations similar to those given in Eq. 31 can be derived for  $\partial^2 \xi_i / \partial \eta_2 \partial \eta_3$  and  $\partial^2 \xi_i / \partial \eta_3 \partial \eta_1$  ( $i=1, \dots, 3$ ). Solving Eq. 31 with the Jacobian matrix of the deformed host geometry, all second order derivatives of the transformed slave mesh can be determined.

## References

- Ackerman, M.J.: The visible human project. Proc IEEE 86 (1998) 504–511
- Barr, A.H.: Global and local deformations of solid primitives. ACM Comput Graph 18(3) (1984) 21–30
- Bradley, C.P.; Pullan, A.J.; Hunter, P.J.: Geometric modeling of the human torso using cubic hermite elements. Ann Biomed Eng 25 (1997) 96–111
- Christie, R.G.: (1997) Numerical modeling of fibre-reinforced thermoplastic sheet forming. PhD thesis, University of Auckland
- Coquillart, S.: Extended free-form deformation: a sculpturing tool for 3D geometric modeling. ACM Comput Graph 24(4) (1990) 187–196
- Dong, F.; Clapworthy, G.; Krokos, M.; Yao, J.: An anatomy based approach to human muscle modeling and deformation. IEEE Trans Visual Comput Graph 8 (2002) 154–170
- Farin, G.: Curves and surfaces for computer aided geometric design. A practical guide, 3rd edn. Academic Press, San Diego, CA (1993)
- Hirota, G.: An improved finite element contact model for anatomical simulations. PhD thesis, University of North Carolina (2002)
- Hsu, W.M.; Hughes, J.F.; Kaufman, H.: Direct manipulation of free-form deformations. ACM Comput Graph 26 (1992) 177–184



- Hunter, P.; Borg, T.K.:** Integration from proteins to organs: the Physiome Project. *Nature Rev. Mol Cell Biology* 4 (2003) 237–243
- Hunter, P.; Robbins, P.; Noble, D.:** The IUPS Human Physiome Project. *Eur J Physiol* 445 (2002) 1–9
- Kalra, P.; Mangili, A.; Magnenat-Thalman, N.; Thalman, D.:** Simulation of facial muscle actions based on rational free-form deformations. *Comput Graph Forum* 2(3) (1992) 59–69
- Maquet, P.G.J.:** Biomechanics of the knee. With application to the pathogenesis and the surgical treatment of osteoarthritis. Springer, Berlin Heidelberg New York (1984)
- Moccozet, L.; Magnenat-Thalman, N.:** Dirichlet free form deformations and their applications to hand simulation. In: *Proceedings of Computer Animation “97”*, Geneva, Switzerland. IEEE Computer Society Press, Los Alimitos, CA (1997) 93–102
- Nielsen, P.M.F.; LeGrice, I.J.; Smaill, B.H.; Hunter, P.J.:** Mathematical model of geometry and fibrous structure of the heart. *Am J Physiol Heart Circ Physiol* 260 (1991) H1365–H1378
- Rusinkiewicz, S.; Levoy, M.:** Efficient variants of the ICP algorithm. In: *Proceedings of the Third International Conference on 3-D digital imaging and modeling (3DIM 2001)*, Quebec City, Canada. IEEE Computer Society Press, Los Alimitos, CA (2001) 145–152
- Schroder, P.; Zorin, D.:** Subdivision for modeling and animation. *Course Notes of SIGGRAPH 98*. ACM SIGGRAPH. (1998) <http://citeseer.nj.nec.com/oder98subdivision.html>
- Sederberg, T.W.; Parry, S.R.:** Free-form deformation of solid geometric models. *ACM Comput Graph* 20(4) (1986) 151–160
- Spitzer, V.M.; Whitlock, D.G.:** The visible human dataset: the anatomical platform for human simulation. *Anat Rec (New Anat)* 253 (1998) 49–57
- Stadler, M.; Holzapfel, G.A.; Korelc, J.:**  $C^n$  continuous modeling of smooth contact surfaces using NURBS and application to 2D problems. *Int J Num Meth Eng* 57 (2003) 2177–2203
- Stevens, C.:** An anatomically-based computational study of cardiac mechanics and myocardial infarction. PhD thesis, University of Auckland, New Zealand (2002)
- Wriggers, P.; Krstulovic-Opapa, L.; Korelc, J.:** Smooth  $C^1$ -interpolations for two-dimensional frictional contact problems. *Int J Num Meth Eng* 51 (2001) 1469–1495
- Young, A.A.; Hunter, P.J.; Smaill, B.H.:** Epicardial surface estimation from coronary angiograms. *Comput Vis Graph Image Process* 47 (1989) 111–127